ARTICLES
https://doi.org/10.1038/s41556-017-0028-5
nature cell biology

Local control of intracellular microtubule dynamics by EB1 photodissociation

Jeffrey van Haren[1], Rabab A. Charafeddine[1], Andreas Ettinger[1,3], Hui Wang[2], Klaus M. Hahn[2] and Torsten Wittmann[1]*

End-binding proteins (EBs) are adaptors that recruit functionally diverse microtubule plus-end-tracking proteins (+TIPs) to growing microtubule plus ends. To test with high spatial and temporal accuracy how, when and where +TIP complexes contribute to dynamic cell biology, we developed a photo-inactivated EB1 variant (π-EB1) by inserting a blue-light-sensitive protein–protein interaction module between the microtubule-binding and +TIP-binding domains of EB1. π-EB1 replaces endogenous EB1 function in the absence of blue light. By contrast, blue-light-mediated π-EB1 photodissociation results in rapid +TIP complex disassembly, and acutely and reversibly attenuates microtubule growth independent of microtubule end association of the microtubule polymerase CKAP5 (also known as ch-TOG and XMAP215). Local π-EB1 photodissociation allows subcellular control of microtubule dynamics at the second and micrometre scale, and elicits aversive turning of migrating cancer cells. Importantly, light-mediated domain splitting can serve as a template to optically control other intracellular protein activities.

Microtubules (MTs) self-organize to form polarized arrays of dynamic intracellular tracks, enabling directional transport, chromosome segregation and cell polarity. MT network remodelling through stochastic switching of dynamic MT plus ends between phases of growth and shortening and selective stabilization is critical for all MT functions in cells. Despite extensive biochemical insights from in vitro experiments and computational models[1], how MT dynamics are locally controlled inside cells is incompletely understood. In addition, how local control of MT dynamics contributes to complex cell and tissue morphogenesis remains unclear, which represents a gap in our understanding of physiological MT function. Interactions of growing MT plus ends with other intracellular components are mediated by a class of proteins referred to as microtubule plus-end-tracking proteins (+TIPs)[2,3]. Association of most, if not all, +TIPs with growing MT ends requires end-binding proteins (EBs), in particular, EB1 (encoded by *MAPRE1*) and EB3 (encoded by *MAPRE3*) in mammalian cells. Although EBs associate with all growing MT ends, the composition of the EB-recruited +TIP complex is tightly controlled in cells in space and time[4–9]. In addition, different +TIP complexes can have antagonistic effects. EBs can recruit enzymes to growing MT ends, promoting either MT polymerization[7] or depolymerization[10], and how these opposing activities are balanced remains unknown. Here, we developed a strategy to inactivate the +TIP adaptor EB1 by light, a stimulus that can be controlled with high spatial and temporal accuracy and is compatible with high-resolution microscopy of cell dynamics. We demonstrate that a photo-inactivated EB1 variant (π-EB1) allows accurate control of intracellular MT dynamics and function, allowing new experimental paradigms and serving as proof of principle of a new optogenetic protein inactivation design.

Results

Design of a photo-inactivated EB1 variant. EB1 consists of two functional domains. The amino-terminal CH domain recognizes growing MT ends[11,12], whereas the carboxy-terminal EBH domain recruits +TIPs[13]. We predicted that controlling their connection using light would disrupt EB1-mediated +TIP interactions with growing MT ends, without interfering with EB1 binding to MTs. Unlike most other optogenetic reagents in which light induces protein–protein interactions[14], the protein A Z-domain-derived affibody, Zdk1 (ref.[15]), functions the opposite way and binds to the oat phototropin 1 LOV2 domain with high affinity in the dark, but dissociates in blue light (Fig. 1a). To develop a light-sensitive EB1 variant, we inserted the LOV2–Zdk1 module into the intrinsically disordered linker between the N-terminal and C-terminal EB1 domains. Because efficient EB1 plus-end tracking requires dimerization[16,17], we further inserted a GCN4 leucine zipper between the CH and LOV2 domains to retain dimerization and plus-end tracking of the N-terminal half by itself. We refer to these photo-inactivated π-EB1 constructs as EB1N-LOV2 and Zdk1-EB1C (Fig. 1b). Affinity-purified glutathione *S*-transferase (GST)-tagged EB1N-LOV2 bound poly-histidine (6xHis)-tagged Zdk1-EB1C and precipitated both SxIP motif (CLIP-associated protein 2 (CLASP2)) and CAP-Gly motif ($p150^{Glued}$) +TIPs from cell lysates. This indicates that the two π-EB1 halves interact and that Zdk1-EB1C is functional in binding known classes of +TIPs (Supplementary Fig. 1a). To directly visualize π-EB1 dynamics in cells and because tagging EB1 at either the N terminus or the C terminus interferes with EB1 function[18], we inserted an enhanced green fluorescent protein (eGFP) tag N-terminal to the Zdk1 peptide. To initially test the π-EB1 light response, the LOV2 domain was photoactivated by turning on the 488 nm acquisition channel, which represents saturating blue light exposure. eGFP-Zdk1-EB1C was recruited to MT ends by non-tagged EB1N-LOV2, and dissociated from MT ends in response to blue light with a half-life ($t_{½}$) of <200 ms (Fig. 1c,d), which is close to the diffusion-limited turnover time of EB1 molecules on MT ends[19,20]. Zdk1-EB1C remained enriched near centrosomes that bind SxIP-motif +TIPs independent of growing MT ends[21]. Because Zdk1 binding requires the LOV2 C terminus, we further inserted mCherry between EB1N and LOV2 to verify that the π-EB1 N-terminal half remained on growing MT ends (Fig. 1e,f).

[1]Department of Cell and Tissue Biology, University of California, San Francisco, CA, USA. [2]University of North Carolina, Chapel Hill, NC, USA. Present address: [3]Institute of Epigenetics and Stem Cells, Helmholtz Center Munich, München, Germany. *e-mail: torsten.wittmann@ucsf.edu

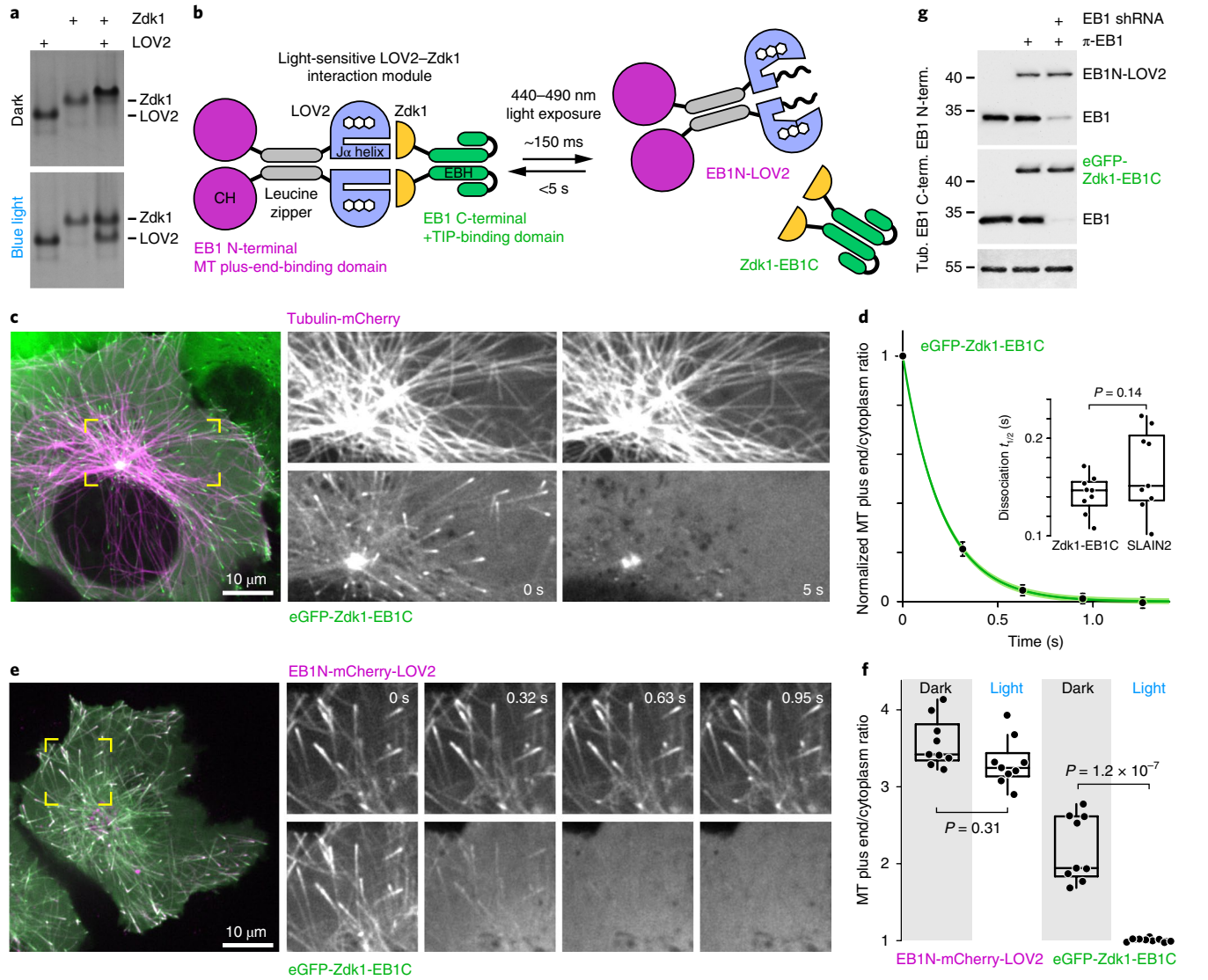

Fig. 1 | Design of a light-sensitive EB1 variant that can replace endogenous EB1 function. a, Interaction of purified LOV2 and Zdk1 analysed by native polyacrylamide gel electrophoresis (PAGE). Blue light results in dissociation of the LOV2–Zdk1 complex, which is upshifted compared with the individual proteins. **b**, Schematic of the photo-inactivated π-EB1 design resulting in reversible dissociation of the MT-binding and +TIP adaptor domains upon blue light exposure. **c**, Cell expressing tubulin-mCherry, eGFP-tagged Zdk1-EB1C and unlabelled EB1N-LOV2 before and after 5 s of 488-nm blue light exposure, resulting in dissociation of Zdk1-EB1C from growing MT plus ends. **d**, Analysis of the blue-light-induced eGFP-Zdk1-EB1C dissociation rate from MT ends. Data shown are the mean ± 95% confidence intervals of $n = 9$ cells. The solid line is an exponential decay fit. Inset shows comparison of dissociation half-life times of Zdk1-EB1C and SLAIN2, which is a +TIP that depends on EB1 for MT end association. Statistical analysis by two-tailed *t*-test. **e**, Cell expressing both π-EB1 halves with different fluorescent tags, showing that EB1N-LOV2 remains on growing MT ends after blue light exposure. Time stamps indicate the duration of blue light exposure. Dual-wavelength images were acquired simultaneously using an emission image splitter. **f**, Analysis of the amount of the two π-EB1 halves bound to MT ends before and during 1 s of blue light exposure. $n = 9$ cells. Statistical analysis by Tukey–Kramer honest significant difference (HSD) test. **g**, Analysis of EB1 and π-EB1 expression in H1299 cell lines in which π-EB1 constructs were stably expressed and endogenous EB1 depleted by shRNA. Immunoblots were probed with antibodies against either the EB1 N terminus or the C terminus and anti-α-tubulin as loading control. Experiments in **a** and **g** were replicated three times with similar results. Yellow boxes in **c** and **e** indicate regions shown as individual channels at higher magnification. Box plots in **d** and **f** show median, first and third quartile, with whiskers extending to observations within 1.5 times the interquartile range, and all individual data points. Unprocessed original blots are shown in Supplementary Fig. 5. Source data are shown in Supplementary Table 3.

These data demonstrate that both halves of π-EB1 are recruited to MT ends efficiently in the dark, and that blue light induces rapid π-EB1 photodissociation.

Acute and reversible +TIP complex disruption by π-EB1 photodissociation. To analyse the functional consequences of π-EB1 photodissociation, we generated cell lines in which endogenous EB1 activity was largely replaced by π-EB1. We chose H1299 non-small-cell lung cancer cells because they express almost no EB3 (ref. [22]) (Supplementary Fig 1c). We first made H1299 cell lines that stably expressed π-EB1 constructs. Even though both π-EB1 halves were expressed from different plasmids, selecting clonal lines that show normal MT plus-end association of eGFP-Zdk1-EB1C, which requires untagged EB1N-LOV2 to be present, resulted in H1299 cell lines with both π-EB1 halves at similar and near endogenous levels (46 ± 17% EB1N-LOV2; 29 ± 11% eGFP-Zdk1-EB1C

compared with endogenous EB1; $n=4$). Next, endogenous EB1 was depleted in π-EB1-expressing cells by lentivirus-mediated short hairpin RNA (shRNA) by ~90±2% ($n=3$) (Fig. 1g). These π-EB1/EB1 shRNA cells used in subsequent experiments were viable with no obvious phenotype, indicating that π-EB1 expression rescues loss of endogenous EB1 function.

We then asked how π-EB1 photodissociation affected the dynamics of mCherry-tagged +TIPs at growing MT ends. All +TIPs that were tested localized to MT plus ends in non-illuminated cells, but disappeared rapidly from MT ends during blue light exposure, confirming that MT end association of mitotic centromere-associated kinesin (MCAK; also known as KIF2C), CLASP2 and SLAIN motif-containing protein 2 (SLAIN2) critically depends on interactions with the C-terminal domain of EB1 (Fig. 2a). In addition, +TIP dissociation was reversible over multiple cycles of light exposure (Fig. 2b and Supplementary Video 1), indicating that π-EB1 photodissociation rapidly and reversibly disrupts the MT plus-end +TIP complex. +TIPs only dissociated from growing MT ends and not from other binding sites; for example, CLASP2 remained at the Golgi apparatus[23] (Supplementary Fig. 2a), demonstrating that +TIP dissociation from MT ends is specific to the light-sensitive π-EB1 dissociation. EB3-mCherry also partially dissociated from MT ends upon π-EB1 photodissociation, which probably reflects heterodimerization with π-EB1 and supports a dominant effect of π-EB1 photodissociation even in the presence of small amounts of endogenous EBs[17,24] (Supplementary Fig. 2b).

Subcellular spatial control of π-EB1 photodissociation. Because EB1 diffuses freely through the cytoplasm[20], spatial control requires rapid re-association of photodissociated π-EB1 molecules in the absence of blue light to prevent diffusion throughout the cell. Compared with wild-type (WT) LOV2, π-EB1 containing the LOV2 (I427V) variant with faster dark-state recovery[15,25] re-associated on growing MT ends approximately twice as fast (Fig. 2c). To minimize blue-light-induced phototoxicity, we determined the minimum dosage of blue light exposure required for sustained π-EB1 photodissociation. To achieve a range of radiant exposures, we used pulse-width modulation of a 470 nm LED (0.25–20-ms pulse lengths) at a fixed irradiance and a pulse frequency of 1 Hz between camera exposures (Fig. 2d). Compared with WT LOV2, the faster LOV2 domain required approximately three-times more blue light to reach the same steady-state π-EB1 photodissociation. Thus, faster LOV2 dark recovery comes at a cost of increased dosage of blue light exposure. To test how this blue light exposure related to typical fluorescence microscopy light levels[26], we compared π-EB1 photodissociation with images of mEmerald-tagged tubulin at identical exposure settings (Supplementary Fig. 2c), indicating that π-EB1 photodissociation-associated photodamage is probably small.

Next, we used a digital micromirror device mask to test whether LOV2 kinetics are sufficient for localized π-EB1 photodissociation. With the faster LOV2 variant, 20-ms 470-nm light pulses of <1 mJ mm^{-2} every second achieved intracellular gradients with 95% difference in π-EB1 photodissociation over a width of ~20 µm (Fig. 2e,f), and reversibly switched π-EB1 photodissociation between different intracellular regions (Fig. 2g and Supplementary Video 2). The photodissociation boundary was similar to the edge steepness of the illumination pattern (Fig. 2f), which was much shallower than expected from the theoretical resolution limit. Thus, boundary steepness was mostly determined by the sharpness of the illumination pattern edge, which is a potential technical limit, and to a lesser extent by diffusion of photodissociated molecules out of the blue-light-exposed region. Because WT LOV2 achieved a boundary that was almost as steep at reduced blue light exposure, we continued to use π-EB1/EB1 shRNA cells expressing WT LOV2 π-EB1 and in which endogenous EB1was stably depleted by shRNA.

Acute and local inhibition of MT growth and organization by π-EB1 photodissociation. Many EB1-recruited +TIPs influence MT polymerization dynamics[3], but it is not understood how potentially antagonistic +TIP activities are integrated and spatially controlled inside cells. Although previous EB1/3 short interfering RNA depletion studies demonstrated MT dynamics defects[17,27], such experiments are confounded by indirect and adaptive mechanisms in genetically depleted cells and cannot directly address protein actions in real time. Thus, we tested how π-EB1 photodissociation acutely altered MT dynamics and organization. As expected, the MT-binding half of π-EB1 remained on growing MT ends following π-EB1 photodissociation (Fig. 1e). However, after a few seconds, EB1N-mCherry-LOV2 comet length decreased (Supplementary Fig. 4d,e), which is indicative of a decreased MT growth rate[28]. Indeed, computational tracking of EB1N-mCherry-LOV2 revealed an overall attenuation of MT growth and a reduction in the number of growing MT ends within 30 s of blue light exposure (Fig. 3a,b and Supplementary Video 3), and the shift in the frame-to-frame growth rate distribution indicated that π-EB1 photodissociation predominantly affected fast-growing MT ends (Fig. 3c). Importantly, these changes were reversible, and MT dynamics recovered within minutes of terminating blue light exposure (Fig. 3b). Moreover, the fast kinetics of π-EB1 photodissociation allowed locally restricted inhibition of MT growth (Fig. 3d and Supplementary Video 4). Kymograph analysis indicated that polymerization of individual MT ends did not slow gradually. Instead, MTs abruptly switched to a slower growth rate or underwent a catastrophe following π-EB1 photodissociation (Fig. 3e). However, this response was not always immediate and resulted in a decay of the MT population growth rate with $t_{½}=$~5 s (Fig. 3f), which is at least an order of magnitude slower than π-EB1 photodissociation itself (Fig. 1d). Together, these data demonstrate that the +TIP-recruiting activity of EB1 is acutely required and sufficient to sustain fast and persistent MT growth in interphase cells.

We then tested whether the observed MT growth inhibition was sufficient to reorganize the intracellular MT network. Although difficult to quantify precisely, the density of the peripheral MT network dropped rapidly during blue light exposure, and recovered within minutes after terminating blue light exposure (Fig. 4a). A decrease in the amount of MT polymer was further supported by a robust increase in cytoplasmic tubulin-mCherry fluorescence, which reached a new equilibrium in <1 min ($t_{½}=$~12 s; Fig. 4b) as individual MTs depolymerized in response to π-EB1 photodissociation (Fig. 4c and Supplementary Video 5). Interestingly, two distinct MT populations responded differently. Many radial MTs underwent catastrophes and depolymerized within seconds of π-EB1 photodissociation (Fig. 4d), which is consistent with the observed delay in growth rate attenuation (Fig. 3f). By contrast, a population of more-curvy MTs appeared more resistant to π-EB1 photodissociation, indicating stabilization by mechanisms that no longer require a growth-promoting +TIP complex. To focus on the population of 'pioneer' MTs that grow towards the leading edge of migrating cells[29], we expressed constitutively active Rac1(Q61L) in π-EB1 cells, which induces isotropic leading-edge F-actin polymerization, and exposes fast MT growth that counter-balances retrograde F-actin flow[30]. Local π-EB1 photodissociation resulted in a dramatic retraction of these MTs from Rac1(Q61L)-induced lamellipodia (Fig. 4e and Supplementary Video 6), indicating that EB1-recruited +TIP complexes maintain fast 'pioneer' MT growth near a migrating cell's leading edge. Importantly, by using patterned blue light exposure, intracellular asymmetry of MT network organization could be generated rapidly and maintained for extended periods of time.

EB1 is not required to recruit the MT polymerase CKAP5 to MT ends. Because CKAP5 accelerates MT growth in vitro[2,31] and can bind to the EB-dependent +TIP SLAIN2 (ref.[7]), we hypothesized

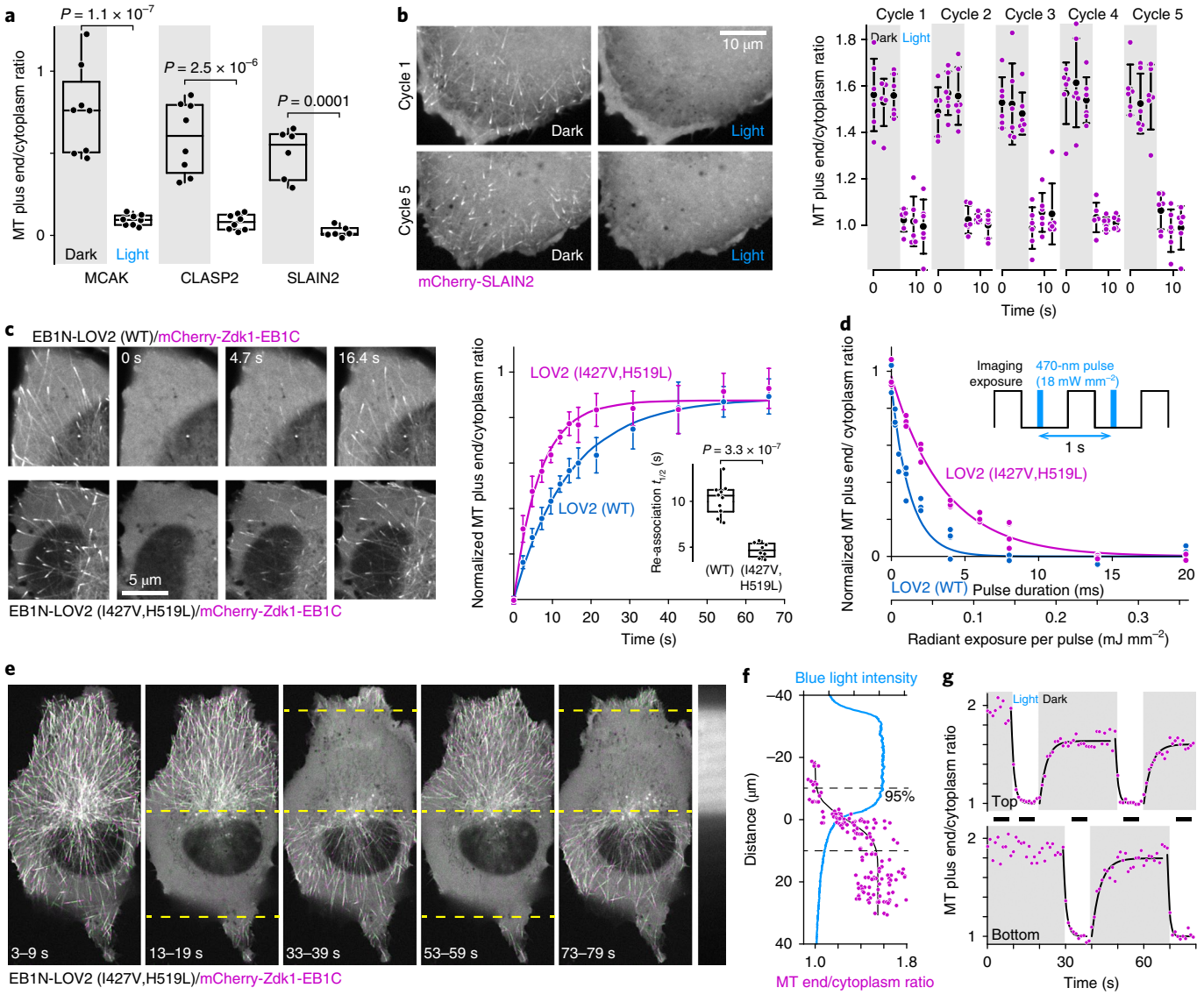

Fig. 2 | Spatially and temporally reversible photodissociation of +TIP complexes. a, Analysis of mCherry-tagged +TIPs on MT ends before and during 1 s of blue light exposure in π-EB1/EB1 shRNA cells. $n = 8$ cells (MCAK and CLASP2) and $n = 6$ cells (SLAIN2). Statistical analysis by Tukey–Kramer HSD test. **b**, Reversible blue-light-induced mCherry-SLAIN2 dissociation from MT ends in π-EB1/EB1 shRNA cells. The graph shows the mean ± standard deviation and individual measurements from the cell shown over multiple cycles of blue light exposure. **c**, Comparison of Zdk1-EB1C recovery on MT plus ends in cells expressing π-EB1 containing the indicated LOV2 variant. The graph compares Zdk1-EB1C re-association with LOV2 (WT) ($n = 10$ cells) or LOV2 (I427V,H519L) ($n = 8$ cells) showing the mean ± 95% confidence intervals. Solid lines are exponential curve fits. Statistical analysis by two-tailed *t*-test. **d**, Zdk1-EB1C MT plus-end association in π-EB1 constructs with the indicated LOV2 variants as a function of radiant exposure at steady state after 40 s of pulsed blue light. Exposure was varied by pulse-width modulation. Solid lines are exponential curve fits. **e**, Patterned blue light exposure within the regions indicated by dashed lines shows high spatiotemporal accuracy of π-EB1 photodissociation. The light pattern is switched every 10 s. Images are projections of the indicated time periods (black bars in **g**) that show sequential time points in alternating green and purple. Right panel: blue light pattern reflected off the cover glass. **f**, Zdk1-EB1C MT plus-end association at the boundary of the blue light pattern corresponding to the 33–39-s period. Dashed lines demarcate the 95% switch (that is, ±2 standard deviations) in MT end association calculated from a cumulative normal distribution fit (black line). The intensity profile of the light pattern (blue line) was measured from the pattern image in **e**. **g**, Zdk1-EB1C MT plus-end association as a function of time in the top and bottom halves of the cell in **e**. Solid lines are exponential curve fits. Shaded areas indicate time periods without blue light exposure. Box plots in **a** and **c** show median, first and third quartile, with whiskers extending to observations within 1.5 times the interquartile range, and all individual data points. Source data are shown in Supplementary Table 3.

that loss of CKAP5 from MT ends in response to π-EB1 photodissociation may cause the observed MT growth inhibition. Consistent with previous reports, mKate2-tagged CKAP5 localized to dynamic dots at distal MT ends[32,33]. However, even in control cells, only a subset of EB1 comets had associated dots of CKAP5-mKate2 (Fig. 5a), and CKAP5-mKate2 was often completely absent from elongated EB1 comets on fast-growing MT ends (Fig. 5b). In addition, quantitative comparison revealed no clear correlation between the amount of EB1 and CKAP5 associated with the same MT plus ends (Fig. 5c). We then tested whether π-EB1 photodissociation altered intracellular CKAP5 dynamics: even after 30 s of blue light exposure, when persistent MT growth has ceased, the relative brightness of CKAP5 dots did not significantly decrease (Fig. 5d–f and Supplementary Video 7).

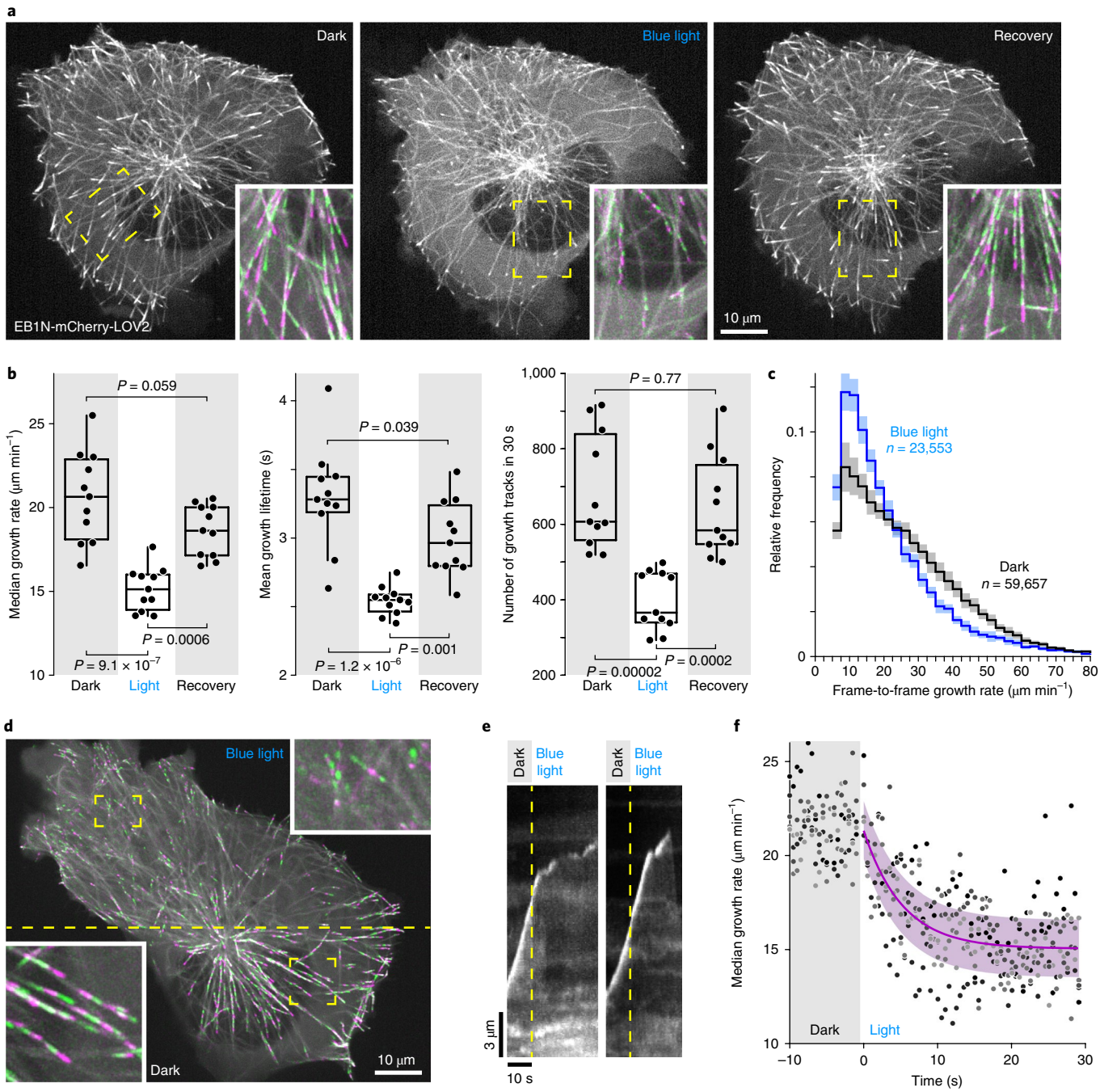

Fig. 3 | Attenuation of MT growth by π-EB1 photodissociation. a, EB1N-mCherry-LOV2-labelled MT plus ends before blue light exposure, after 30 s during blue light exposure and after 3-min recovery in the dark in π-EB1/EB1 shRNA cells. Insets show maximum intensity projections over 20-s time windows of the indicated regions at higher magnification. **b**, Quantification of MT polymerization dynamics by tracking EB1N-mCherry-LOV2-labelled MT ends. Growth rates are frame-to-frame measurements from images acquired at 0.5-s intervals. $n = 11$ cells. Box plots show median, first and third quartile, with whiskers extending to observations within 1.5 times the interquartile range, and all individual data points. Statistical analysis by Tukey–Kramer HSD test. **c**, Comparison of the frame-to-frame MT growth rate distribution in the dark and during blue light exposure, demonstrating a specific loss of fast growth events as a result of π-EB1 photodissociation. Shown are the mean distributions from the cells in **b** (lines) and the 95% confidence intervals (shaded areas). **d**, Local inhibition of MT growth by patterned blue light exposure in a π-EB1/EB1 shRNA cell expressing EB1N-mCherry-LOV2. Shown is a maximum intensity projection over 20 s. Only the top half above the dashed line was exposed to blue light pulses between image acquisitions. Insets show the indicated regions at higher magnification. This experiment was replicated more than five times with similar results. **e**, Representative kymographs illustrating the sudden response of rapidly growing MT ends to π-EB1 photodissociation. **f**, Analysis of the intracellular MT population growth rate response as a function of time after π-EB1 photodissociation. Shown are all measurements from $n = 5$ cells. The purple solid line is an exponential fit of the mean during blue light exposure. The purple shaded area is the 95% confidence interval of the fit. In **a** and **d**, sequential time points in maximum intensity projections are shown in alternating green and purple to better visualize MT growth tracks. Source data are shown in Supplementary Table 3.

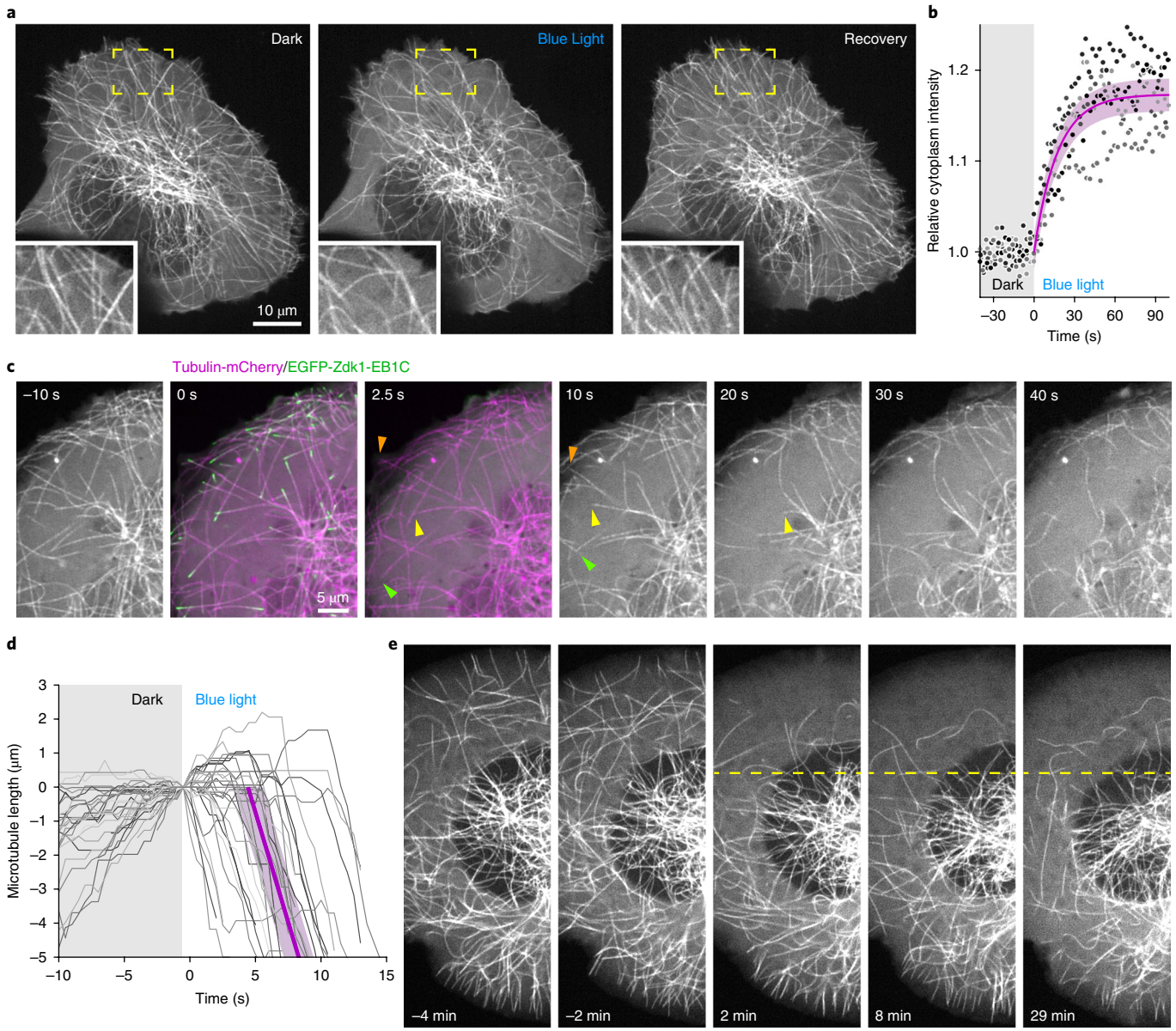

Fig. 4 | π-EB1 photodissociation-induced MT cytoskeleton reorganization. a, Tubulin-mCherry expressing π-EB1/EB1 shRNA cell before blue light exposure, after 30 s during blue light exposure and after 3-min recovery in the dark. Insets show the indicated regions at higher magnification, demonstrating reversible decrease of MT density near the cell periphery. **b**, Analysis of the relative amount of cytoplasmic tubulin-mCherry in response to π-EB1 photodissociation. Shown are all measurements from $n = 5$ cells normalized to the dark condition. The purple solid line is an exponential fit of the mean during blue light exposure. The purple shaded area is the 95% confidence interval of the fit. **c**, Rapid depolymerization of MTs in the cell periphery in response to π-EB1 photodissociation. Different coloured arrowheads highlight different representative MTs. **d**, Life-history plots of MTs with ends near the cell edge aligned to the time of the start of blue light exposure. $n = 33$ MTs from 5 cells. The purple line is the average of the linear fits of the depolymerizing phase of these MTs. The purple shaded area indicates the 95% confidence interval. **e**, Time-lapse sequence of tubulin-mCherry in a Rac1(Q61L)-expressing π-EB1 cell in response to local blue light exposure (above the dashed line), illustrating sustained reorganization of the MT network. This experiment was replicated more than five times with similar results. Source data are shown in Supplementary Table 3.

Because we were concerned about incomplete and variable EB1 depletion by shRNA, we next deleted the genes encoding EB1 and EB3 (EB1/3$^{-/-}$) in H1299 cells by CRISPR–Cas9 genome editing (Supplementary Fig. 3a). This eliminated both EB1 and potentially compensatory EB3 expression (Supplementary Fig. 3b,c) and EB-dependent +TIP recruitment (Supplementary Fig. 3d). Nevertheless, even in these genetically deleted EB1/3$^{-/-}$ cells, CKAP5-mKate2 still associated with growing MT ends (Supplementary Fig. 3e and Supplementary Video 8). In addition, MT growth was inhibited in EB1/3$^{-/-}$ cells and indistinguishable from what we observed in blue-light-exposed π-EB1-expressing EB1 shRNA cells (Fig. 5g). Importantly, both in EB1 shRNA cells and in EB1/3$^{-/-}$ cells, only expression of both π-EB1 halves (Supplementary Fig. 4a,b) rescued MT growth rate and comet length in a light-dependent manner (Fig. 5h, Supplementary Video 9 and Supplementary Fig. 4c–e), but expression of the N-terminal MT-binding half alone, EB1N-mCherry-LOV2, did not (Fig. 5g). CKAP5-mKate2 associated with a population of growing MT ends in EB1/3$^{-/-}$ π-EB1 rescue cells both in the dark and during blue light exposure (Supplementary Fig. 4f). Together, these data demonstrate that CKAP5 MT plus-end association is independent of EB1-mediated +TIP recruitment, and therefore cannot explain MT growth inhibition by π-EB1 photodissociation.

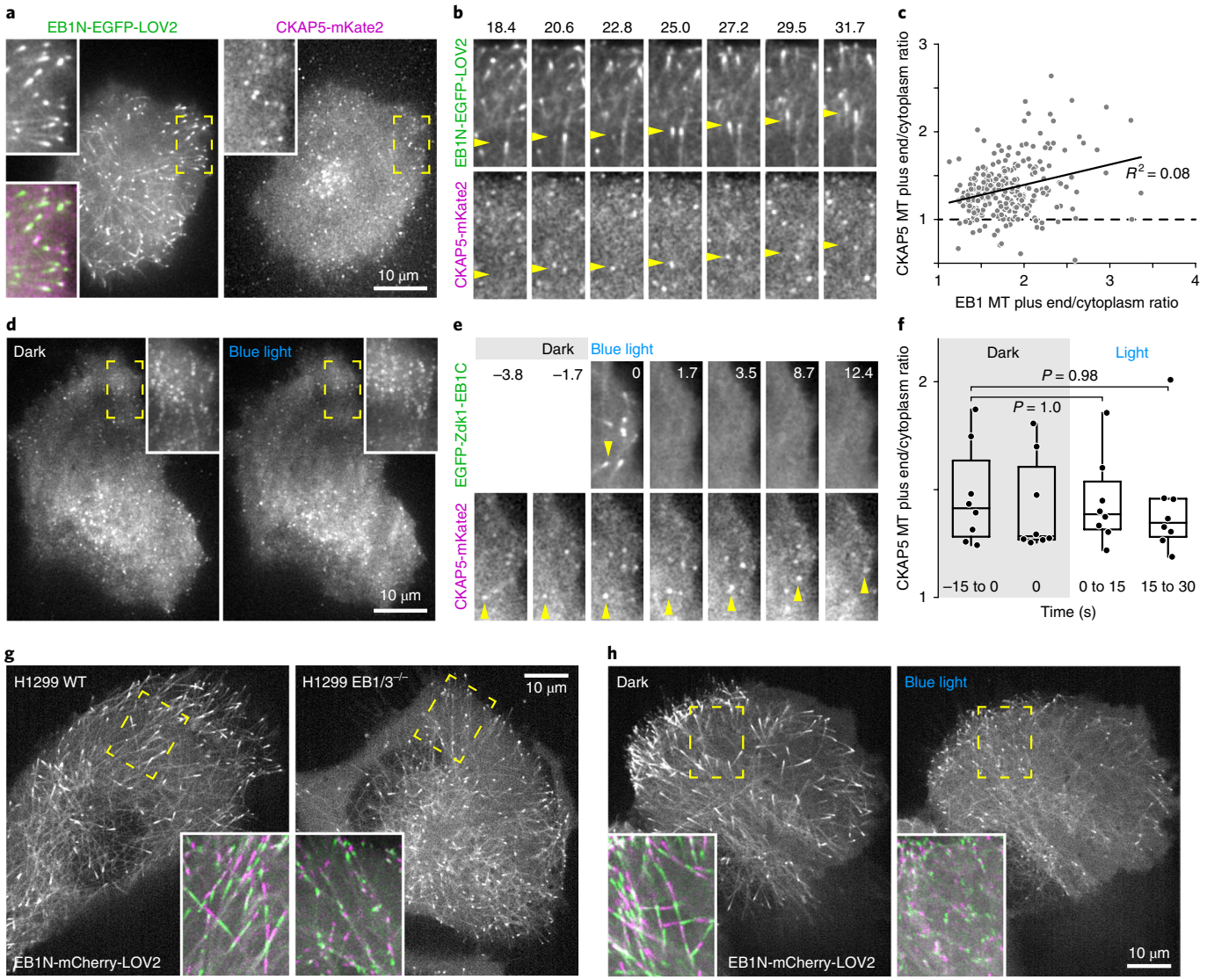

Fig. 5 | EB1-independent MT plus-end localization of the MT polymerase CKAP5. a, TIRF microscopy of a control H1299 cell expressing EB1N-eGFP-LOV2 and CKAP5-mKate2. CKAP5 forms dots at growing MT ends that are unlike the typical comet-shaped EB1 distribution. Note that wavelengths were acquired sequentially, resulting in a small temporal shift between channels. Insets show indicated regions at higher magnification. **b**, Time-lapse sequence showing variable and transient CKAP5 accumulation on MT ends. Arrowheads highlight representative MT ends. Elapsed time is shown in seconds. **c**, Scatter plot of the relative accumulation of CKAP5 and EB1 on the same MT ends showing only a very weak correlation. The dashed line indicates the ratio of 1 at which no MT end accumulation of CKAP5-mKate2 can be detected. The solid line is a linear fit. $n = 252$ MT ends from 5 cells. **d**, TIRF microscopy of CKAP5-mKate2 in a π-EB1/EB1 shRNA cell 15 s before (left panel) and during (right panel) π-EB1 photodissociation, showing qualitatively indistinguishable CKAP5 distribution. Insets show projections over 20-s time windows of the indicated regions, revealing linear tracks of CKAP5 dots. **e**, Time-lapse sequence of CKAP5-mKate2 dynamics before and during blue light exposure in a π-EB1/EB1 shRNA cell. Arrowheads highlight the continued linear movement of a MT-end-associated CKAP5 dot. Elapsed time is shown in seconds. **f**, CKAP5 enrichment on MT ends in the indicated time intervals before and during blue light exposure, indicating no change in response to π-EB1 photodissociation. Statistical analysis by Tukey–Kramer HSD test. Box plots show median, first and third quartile, with whiskers extending to observations within 1.5 times the interquartile range, and all individual data points. $n = 8$ cells. **g**, EB1N-mCherry-LOV2-labelled MT plus ends in control H1299 cells and in cells in which both EB1 and EB3 expression were deleted by CRISPR–Cas9 genome editing, showing attenuation of MT growth in EB1/3$^{-/-}$ cells. **h**, EB1N-mCherry-LOV2-labelled MT plus ends in a EB1/3$^{-/-}$ π-EB1 rescue cell before and during blue light exposure, demonstrating light-induced MT growth attenuation very similar to what we observe in π-EB1/EB1 shRNA cells. In **g** and **h**, insets show maximum intensity projections over 20-s time windows of the indicated regions. Sequential time points in these projections are shown in alternating green and purple to better visualize MT growth tracks. Experiments were replicated more than five times with similar results. Source data are shown in Supplementary Table 3.

Local π-EB1 photodissociation induces rapid cell turning. Persistent MT growth towards the leading edge has long been speculated to maintain directional cell migration[34–36]. However, owing to the lack of experimental tools to manipulate intracellular MT dynamics with high spatial and temporal accuracy, the central question to what extent MT network polarity is a cause or consequence of directional migration has not been adequately addressed. Thus, we used our CRISPR EB1/3$^{-/-}$ π-EB1 rescue cells to ask how acute interference with EB-dependent MT plus-end interactions influenced directional cell migration. We focused on randomly migrating single cells in the absence of other chemical or haptotactic cues. As expected, WT H1299 cells did not react to local blue light

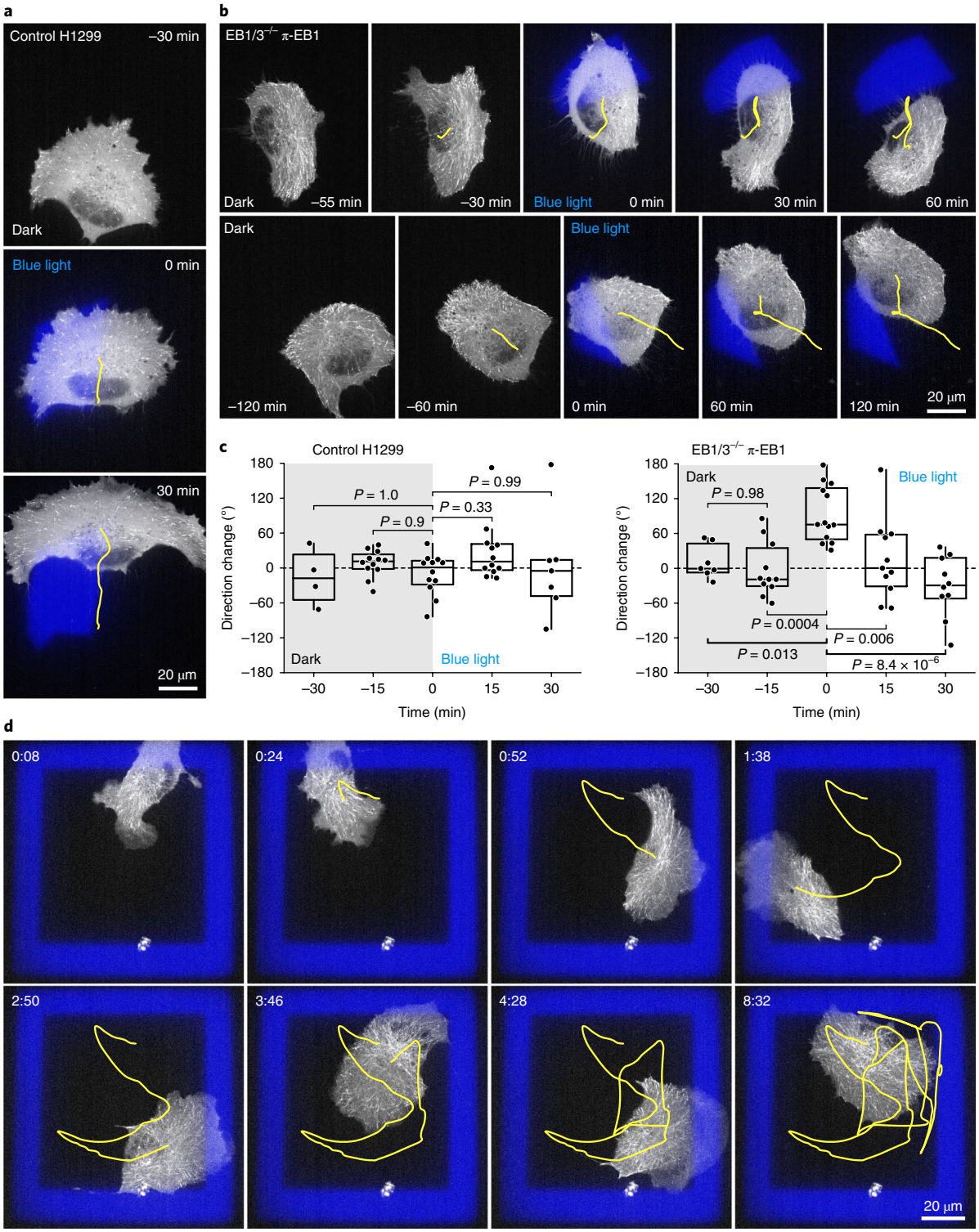

Fig. 6 | Aversive cell turning in response to local π-EB1 photodissociation. a, Time-lapse sequence of a control H1299 cell expressing EB3-mCherry showing no response to local blue light exposure. **b**, Two examples of EB1/3$^{-/-}$ π-EB1 rescue cells that turn away from local blue light exposure in the front half of the cell. Cells also express mCherry-Zdk1-EB1C to show local π-EB1 photodissociation. Blue areas are images of the patterns of blue light exposure reflected off the coverslip. Yellow lines show the cell centroid trajectory. 0 min indicates the time when the respective blue light pattern was switched on. **c**, Analysis of cell migration direction changes over 30-min time intervals expressed as the angle between smoothened centroid positions 15 min before and 15 min after the indicated time points. A significant non-random change in migration direction only occurred in response to local blue light exposure in EB1/3$^{-/-}$ π-EB1 rescue cells, which consistently turned away from the pattern. $n = 12$ cells (control); $n = 13$ cells (EB1/3$^{-/-}$ π-EB1). Dashed line indicates no direction change. Box plots show median, first and third quartile, with whiskers extending to observations within 1.5 times the interquartile range, and all individual data points. Statistical analysis by Tukey–Kramer HSD test. **d**, Time-lapse sequence of a migrating EB1/3$^{-/-}$ π-EB1 rescue cell trapped inside a virtual blue light box for >8 h. The yellow line marks the centroid trajectory. This experiment was replicated more than three times with similar results.

exposure (Fig. 6a). By contrast, EB1/3$^{-/-}$ π-EB1 rescue cells consistently turned away from blue-light-exposed regions that were placed in the front half of a migrating cell (Fig. 6b). Although H1299 cells often switched direction and random protrusion dynamics contributed substantially to centroid trajectory directional noise, in a quantitative comparison of multiple cells, the only significant direction change occurred as a response to local blue light exposure in EB1/3$^{-/-}$ π-EB1 rescue cells (Fig. 6c). We then tested whether this aversive turning response to local π-EB1 photodissociation was sufficient to confine a migrating cell within a predefined region. Indeed, even though these cells are highly motile, EB1/3$^{-/-}$ π-EB1 rescue cells were unable to escape from a blue light box and reversed direction every time the cell touched the virtual blue light barrier for an observation period of >8 h (Fig. 6d and Supplementary Video 10). Thus, EB1-mediated interactions of +TIP complexes with growing MT ends are necessary to maintain leading-edge identity and directionality during cell migration.

Discussion

To locally dissect complex and dynamic cell biology, new methods are needed to rapidly inactivate specific protein activities inside cells. Here, we use the +TIP-recruiting activity of EB1 as a proof of principle to photo-inactivate specific protein functions by inserting a light-sensitive LOV2–Zdk1 protein–protein interaction module between functional domains. Unlike genetic methods that are orders of magnitude too slow to dissect highly dynamic MT and +TIP functions and offer no spatial control, we demonstrate acute, reversible π-EB1 photodissociation and control of intracellular MT dynamics at second and micrometre accuracy inside live cells. In contrast to genetic methods to silence or knockout genes, this approach allows the replacement of a protein of interest with a photo-inactivated π-variant that can be fully characterized for normal function in the absence of blue light. Thus, acute and local photo-inactivation can be used to directly observe and analyse a cellular response, rather than inferring protein function from a cell population in which a gene of interest has been removed and in which cells may have adapted to the loss of function through poorly controlled compensatory mechanisms. In the case of +TIP or other complex protein networks, biochemical competition[37] may further complicate mechanistic interpretation of depletion or knockout phenotypes. To our knowledge, this light-induced reversible domain splitting is the only optogenetic method to allow acute, reversible and specific loss-of-function experiments. Most other optogenetic tools rely on gain of function, in which proteins are activated, relocalized or aggregated by light. There are only a few methods of light-induced protein inactivation that are either slow and irreversible, such as protein depletion by light-induced proteolysis[38] or genome editing[39], or require large a priori knowledge of target protein structure[40].

Acute π-EB1 photodissociation allowed us to obtain new insights into the role of EB1 and the associated +TIP complex in the physiological control of MT dynamics and function. Although we only tested a subset of SxIP-motif +TIPs, recruitment of all known +TIPs depends on interactions with the EB1 C terminus[3,41]. Thus, we think that π-EB1 photodissociation results in a broad disruption of +TIP association with MT ends. In vitro, EB1 stimulates tubulin GTP hydrolysis and increases the catastrophe frequency[12,42,43], but only moderately increases the MT growth rate at high EB1 concentrations. By contrast, we find that in cells, EB1-mediated +TIP complexes maintain fast and persistent MT growth. Thus, the EB1 intrinsic MT-destabilizing activity is outweighed by the growth-promoting activity of the EB1-recruited +TIP complex. Because the N-terminal half of π-EB1 remains on growing MT ends after photodissociation, structural changes induced by EB1 binding[12] are insufficient to maintain persistent MT growth. In contrast to previous reports[17], at physiological expression levels, the N-terminal MT-binding half of EB1 by itself had no noticeable effect on intracellular MT dynamics. The growth-promoting activity of the EB1-mediated +TIP complex also cannot easily be explained by interactions with the canonical MT polymerase CKAP5. CKAP5 association with the most distal tips of MT plus ends does not correlate well with EB1 localization and does not depend on EB1 either in the π-EB1 photodissociation experiments or in cells in which we removed EB1 and EB3 by genome editing. Although this is consistent with EB1-independent CKAP5 localization to MT ends in vitro[31], this was surprising as CKAP5 recruitment to growing MT ends in cells was previously attributed to EB1-mediated interactions with the +TIP SLAIN2 (refs[7,33]), which rapidly disappears from growing MT ends upon π-EB1 photodissociation. In any case, our results show that, in the absence of an EB1-recruited +TIP complex, CKAP5 by itself cannot maintain physiological MT growth, and additional mechanisms that control CKAP5 activity could be involved. Strikingly, individual MTs respond to π-EB1 photodissociation stochastically and often continue to grow for some time before switching abruptly from fast to slow growth, indicating a sudden state change of the growing MT end seconds after +TIP complex dissociation. Thus, alternatively, the +TIP complex may stabilize the protective GTP-like MT end cap[44] in cells independent of CKAP5.

As an example to demonstrate the utility of π-EB1 in interrogating dynamic cell biology, we asked whether local +TIP dissociation is sufficient to influence migration of cancer cells in which we replaced EB1 and EB3 with π-EB1. We find that the response of migrating H1299 non-small-cell lung cancer cells to local π-EB1 photodissociation is remarkably robust: cells invariably turned away from the area of blue light exposure within minutes and were unable to cross a virtual blue light boundary. Thus, even in this highly transformed metastatic cancer cell line, +TIP-mediated MT interactions in the front of the cell are essential to define and maintain directional polarity. This is consistent with our previous finding that cell–matrix-adhesion-associated MT tracks support localized secretion of matrix metalloprotease activity[45], which supports MT involvement in invasive cancer cell migration and emerging ideas that MT-directed cancer chemotherapy targets cell functions other than mitosis[46].

In summary, regardless of the precise mechanism by which EB1-recruited +TIP complexes maintain physiological MT growth rates, our data demonstrate local and acute modulation of intracellular MT dynamics with spatial and temporal accuracy that surpasses recent photopharmacological approaches[47], and together with selective optogenetic recruitment of specific proteins to MT ends[48] will allow precise dissection of +TIP functions in complex cell biology. Finally, insertion of a light-sensitive protein–protein interaction module between functional domains is a powerful strategy applicable to a large fraction of the proteome, enabling new spatially and temporally resolved experimental questions that cannot be addressed by other genetic or pharmacological means.

Methods

Methods, including statements of data availability and any associated accession codes and references, are available at https://doi.org/10.1038/s41556-017-0028-5.

Received: 10 January 2017; Accepted: 13 December 2017;
Published online: 29 January 2018

References

1. Ohi, R. & Zanic, M. Ahead of the curve: new insights into microtubule dynamics. *F1000Res.* **5**, 314 (2016).
2. Akhmanova, A. & Steinmetz, M. O. Control of microtubule organization and dynamics: two ends in the limelight. *Nat. Rev. Mol. Cell. Biol.* **16**, 711–726 (2015).
3. Kumar, P. & Wittmann, T. +TIPs: SxIPping along microtubule ends. *Trends Cell Biol.* **22**, 418–428 (2012).
4. Kumar, P. et al. GSK3beta phosphorylation modulates CLASP–microtubule association and lamella microtubule attachment. *J. Cell. Biol.* **184**, 895–908 (2009).

5. Pemble, H., Kumar, P., van Haren, J. & Wittmann, T. GSK3-mediated CLASP2 phosphorylation modulates kinetochore dynamics. *J. Cell. Sci.* **130**, 1404–1412 (2017).
6. Smyth, J. T. et al. Phosphoregulation of STIM1 leads to exclusion of the endoplasmic reticulum from the mitotic spindle. *Curr. Biol.* **22**, 1487–1493 (2012).
7. van der Vaart, B. et al. SLAIN2 links microtubule plus end-tracking proteins and controls microtubule growth in interphase. *J. Cell. Biol.* **193**, 1083–1099 (2011).
8. van Haren, J. et al. Dynamic microtubules catalyze formation of navigator–TRIO complexes to regulate neurite extension. *Curr. Biol.* **24**, 1778–1785 (2014).
9. Wu, X. et al. Skin stem cells orchestrate directional migration by regulating microtubule–ACF7 connections through GSK3beta. *Cell* **144**, 341–352 (2011).
10. Montenegro, G. S. et al. In vitro reconstitution of the functional interplay between MCAK and EB3 at microtubule plus ends. *Curr. Biol.* **20**, 1717–1722 (2010).
11. Maurer, S. P. et al. EBs recognize a nucleotide-dependent structural cap at growing microtubule ends. *Cell* **149**, 371–382 (2012).
12. Zhang, R., Alushin, G. M., Brown, A. & Nogales, E. Mechanistic origin of microtubule dynamic instability and its modulation by EB proteins. *Cell* **162**, 849–859 (2015).
13. Honnappa, S. et al. An EB1-binding motif acts as a microtubule tip localization signal. *Cell* **138**, 366–376 (2009).
14. Repina, N. A. et al. At light speed: advances in optogenetic systems for regulating cell signaling and behavior. *Annu. Rev. Chem. Biomol. Eng.* **8**, 13–39 (2017).
15. Wang, H. et al. LOVTRAP: an optogenetic system for photoinduced protein dissociation. *Nat. Methods* **13**, 755–758 (2016).
16. Slep, K. C. & Vale, R. D. Structural basis of microtubule plus end tracking by XMAP215, CLIP-170, and EB1. *Mol. Cell.* **27**, 976–991 (2007).
17. Komarova, Y. et al. Mammalian end binding proteins control persistent microtubule growth. *J. Cell. Biol.* **184**, 691–706 (2009).
18. Skube, S. B., Chaverri, J. M. & Goodson, H. V. Effect of GFP tags on the localization of EB1 and EB1 fragments in vivo. *Cytoskelet. (Hoboken)* **67**, 1–12 (2010).
19. Dragestein, K. A. et al. Dynamic behavior of GFP-CLIP-170 reveals fast protein turnover on microtubule plus ends. *J. Cell. Biol.* **180**, 729–737 (2008).
20. Seetapun, D. et al. Estimating the microtubule GTP cap size in vivo. *Curr. Biol.* **22**, 1681–1687 (2012).
21. Yan, X., Habedanck, R. & Nigg, E. A. A complex of two centrosomal proteins, CAP350 and FOP, cooperates with EB1 in microtubule anchoring. *Mol. Biol. Cell.* **17**, 634–644 (2006).
22. Wang, T. et al. Translating mRNAs strongly correlate to proteins in a multivariate manner and their translation ratios are phenotype specific. *Nucleic Acids Res.* **41**, 4743–4754 (2013).
23. Miller, P. M. et al. Golgi-derived CLASP-dependent microtubules control Golgi organization and polarized trafficking in motile cells. *Nat. Cell. Biol.* **11**, 1069–1080 (2009).
24. De Groot, C. O. et al. Molecular insights into mammalian end-binding protein heterodimerization. *J. Biol. Chem.* **285**, 5802–5814 (2010).
25. Christie, J. M. et al. Steric interactions stabilize the signaling state of the LOV2 domain of phototropin 1. *Biochemistry* **46**, 9310–9319 (2007).
26. Ettinger, A. & Wittmann, T. Fluorescence live cell imaging. *Methods Cell. Biol.* **123**, 77–94 (2014).
27. Gierke, S. & Wittmann, T. EB1-recruited microtubule +TIP complexes coordinate protrusion dynamics during 3D epithelial remodeling. *Curr. Biol.* **22**, 753–762 (2012).
28. Bieling, P. et al. CLIP-170 tracks growing microtubule ends by dynamically recognizing composite EB1/tubulin-binding sites. *J. Cell. Biol.* **183**, 1223–1233 (2008).
29. Kaverina, I. & Straube, A. Regulation of cell migration by dynamic microtubules. *Semin. Cell. Dev. Biol.* **22**, 968–974 (2011).
30. Wittmann, T., Bokoch, G. M. & Waterman-Storer, C. M. Regulation of leading edge microtubule and actin dynamics downstream of Rac1. *J. Cell. Biol.* **161**, 845–851 (2003).
31. Brouhard, G. J. et al. XMAP215 is a processive microtubule polymerase. *Cell* **132**, 79–88 (2008).
32. Nakamura, S. et al. Dissecting the nanoscale distributions and functions of microtubule-end-binding proteins EB1 and ch-TOG in interphase HeLa cells. *PLoS. ONE* **7**, e51442 (2012).
33. Bouchet, B. P. et al. Mesenchymal cell invasion requires cooperative regulation of persistent microtubule growth by SLAIN2 and CLASP1. *Dev. Cell.* **39**, 708–723 (2016).
34. Etienne-Manneville, S. Microtubules in cell migration. *Annu. Rev. Cell. Dev. Biol.* **29**, 471–499 (2013).
35. Wittmann, T. & Waterman-Storer, C. M. Cell motility: can Rho GTPases and microtubules point the way? *J. Cell. Sci.* **114**, 3795–3803 (2001).
36. Bouchet, B. P. & Akhmanova, A. Microtubules in 3D cell motility. *J. Cell. Sci.* **130**, 39–50 (2017).
37. Duellberg, C. et al. Reconstitution of a hierarchical +TIP interaction network controlling microtubule end tracking of dynein. *Nat. Cell. Biol.* **16**, 804–811 (2014).
38. Usherenko, S. et al. Photo-sensitive degron variants for tuning protein stability by light. *BMC Syst. Biol.* **8**, 128 (2014).
39. Nihongaki, Y., Kawano, F., Nakajima, T. & Sato, M. Photoactivatable CRISPR–Cas9 for optogenetic genome editing. *Nat. Biotechnol.* **33**, 755–760 (2015).
40. Dagliyan, O. et al. Engineering extrinsic disorder to control protein activity in living cells. *Science* **354**, 1441–1444 (2016).
41. Kumar, A. et al. Short linear sequence motif LxxPTPh targets diverse proteins to growing microtubule ends. *Structure* **25**, 924–932 (2017).
42. Vitre, B. et al. EB1 regulates microtubule dynamics and tubulin sheet closure in vitro. *Nat. Cell. Biol.* **10**, 415–421 (2008).
43. Maurer, S. P. et al. EB1 accelerates two conformational transitions important for microtubule maturation and dynamics. *Curr. Biol.* **24**, 372–384 (2014).
44. Duellberg, C., Cade, N. I., Holmes, D. & Surrey, T. The size of the EB cap determines instantaneous microtubule stability. *eLife* **5**, e13470 (2016).
45. Stehbens, S. J. et al. CLASPs link focal-adhesion-associated microtubule capture to localized exocytosis and adhesion site turnover. *Nat. Cell. Biol.* **16**, 558–573 (2014).
46. Mitchison, T. J. The proliferation rate paradox in antimitotic chemotherapy. *Mol. Biol. Cell.* **23**, 1–6 (2012).
47. Borowiak, M. et al. Photoswitchable inhibitors of microtubule dynamics optically control mitosis and cell death. *Cell* **162**, 403–411 (2015).
48. Adikes, R. C., Hallett, R. A., Saway, B. F., Kuhlman, B. & Slep, K. C. Control of microtubule dynamics using an optogenetic microtubule plus end–F-actin cross-linker. *J. Cell Biol.* **217**, jcb.201705190 (2017).

Acknowledgements

This work was supported by the NIH grants R01 GM079139, R01 GM094819 and S10 RR26758 to T.W., and P41 EB002025 and R35 GM122596 to K.M.H. We thank all members of the Cell and Tissue Biology community for discussions and comments on the manuscript.

Author contributions

J.v.H. and T.W. designed the experiments, analysed the data and wrote the manuscript. J.v.H. performed most of the experiments and generated most of the reagents. A.E. and R.A.C. contributed to reagent generation and experimental work. H.W. and K.M.H. contributed unpublished reagents.

Competing interests

The authors declare no competing financial interests.

Additional information

Supplementary information is available for this paper at https://doi.org/10.1038/s41556-017-0028-5.

Reprints and permissions information is available at www.nature.com/reprints.

Correspondence and requests for materials should be addressed to T.W.

Publisher's note: Springer Nature remains neutral with regard to jurisdictional claims in published maps and institutional affiliations.

Methods

DNA constructs and molecular cloning. mCherry-EB3 was from the Michael Davidson Plasmid Collection (Addgene plasmid 55037). mCherry-CLASP2γ was cloned by replacing the AgeI/KpnI restriction fragment of peGFP-CLASP2γ[49] with the corresponding fragment of pmCherry-C1. Similarly, mCherry-MCAK was cloned by replacing the AgeI/BsrGI fragment of mEmerald-MCAK (Addgene plasmid 54161, from the Michael Davidson Plasmid Collection) with the corresponding fragment of pmCherry-C1. mCherry-α-tubulin was obtained from R. Tsien (Addgene plasmid 49149). PCR-based cloning strategies for other constructs are summarized below, and all primers used are listed in Supplementary Table 2:

(1) EB1N-LZ-LOV2 was constructed as follows: the coding regions corresponding to amino acids 1–185 of an EB1 shRNA-resistant variant[27] and a GCN4 leucine zipper (generated by oligonucleotide assembly PCR) were first amplified, and then connected by overlap extension PCR, and the resulting product ligated into the NheI/XhoI-digested backbone of peGFP-C1. The LOV2 coding sequence originated from PA-Rac1 (Addgene plasmid 22027)[50], and L406/407 A mutations that were reported to stabilize docking of the Jα-helix[51] as well as a GSGSG linker sequence were introduced by PCR. This modified LOV2 domain including the linker was amplified and inserted into the SacII/BamHI sites of the EB1N-LZ plasmid.

(2) EB1N-mCherry-LOV2 was cloned by inserting PCR-amplified mCherry coding sequences into XhoI/SacII sites between LZ and LOV2 in EB1N-LZ-LOV2.

(3) EB1N-eGFP-LOV2 was cloned by inserting the coding sequence for the PCR-amplified GCN4 leucine zipper into the SacII site of EB1N-eGFP-LOV2 by Gibson assembly between eGFP and LOV2.

(4) mCherry-Zdk1-EB1C was cloned in the following way: PCR-amplified mCherry-Zdk1-linker (from pTriEx-mCherry-Zdk1, Addgene plasmid 81057) and the EB1 C-terminal fragment corresponding to amino acids 186–268 were connected by overlap extension PCR. The resulting PCR product was inserted into the NheI/XhoI sites of peGFP-C1. eGFP-Zdk1-EB1C was generated by excising eGFP from peGFP-C1 by restriction digestion with NheI/BsrGI and ligation into NheI/BsrGI-digested mCherry-ZDK1-EB1C, thereby replacing mCherry with eGFP.

(5) GST-EB1N-LZ-LOV2 was cloned by inserting PCR-amplified EB1N-LZ-LOV2 into the BamHI/XmaI sites of pGEX-4T-2 (GE Healthcare Life Sciences).

(6) 6xHis-Zdk1-EB1C was cloned by inserting PCR-amplified ZDK1-EB1C into NheI/XhoI sites of pET28a.

(7) GST-LOV2 was cloned by inserting the PCR-amplified LOV2 coding sequence including a GSGSG linker into BamHI/XhoI sites of pGEX-4T-2.

(8) mCherry-SLAIN2 was cloned by inserting the PCR-amplified SLAIN2 coding sequence into the XhoI/EcoRI sites of pBio-mCherry-C1.

(9) CKAP5-mKate2 was cloned by inserting the PCR-amplified mKate2 coding sequence into the BamHI/NotI sites of chTOG-GFP (Addgene 29480, from L. Wordeman).

Cell culture and generation of π-EB1 cell lines. H1299 human non-small-cell lung cancer cells were cultured in RPMI1640 supplemented with 10% FBS, penicillin/streptomycin and non-essential amino acids at 37 °C, 5% CO_2 in a humidified tissue culture incubator. According to the National Institutes of Health (NIH) guidelines, the identity of H1299 cells was confirmed by short tandem repeat profiling (IDEXX BioResearch) using a standard 9-marker panel: AMEL(X); CSF1PO(12); D13S317(12); D16S539(12,13); D5S818(11); D7S820(10); THO1(6,9.3); TPOX(8); and vWA(16,17,18). The profile obtained was identical to the one reported by the American Type Culture Collection. H1299 cells and derivatives were regularly tested for mycoplasma contamination (IDEXX BioResearch).

π-EB1/EB1 shRNA cells. To replace endogenous EB1 with π-EB1 and to prevent cells from adapting to EB1 depletion, we first generated stable cell lines expressing both halves of an shRNA-resistant variant of π-EB1. H1299 cells were transfected with both untagged EB1N-LOV2 and eGFP-Zdk1-EB1C plasmids and selected with 500 μg ml^{-1} G418. Clones that expressed both halves at comparable expression levels were identified by microscopy, and those colonies in which eGFP-Zdk1-EB1C was clearly localized to growing MT ends, which requires the presence of the unlabelled N-terminal part, were selected. Colonies with a low MT plus end/cytoplasm ratio or displaying strong MT lattice labelling were discarded because expression of both halves was expected to be unequal. Expression of both π-EB1 halves was verified by immunoblot using antibodies that specifically recognize either the EB1 N-terminal (Thermo Fisher Scientific clone 1A11/4) or the C-terminal half (BD Biosciences clone 5/EB1). Next, we knocked down endogenous EB1 in these clones by pLKO.1 lentivirus-mediated shRNA. The EB1 shRNA lentivirus and shRNA-resistant variants were as described previously[27]. Selected colonies were sorted at the UCSF Parnassus Flow Cytometry Core to obtain a homogenous population of cells. π-EB1 cells were then transfected with mCherry-tagged constructs for functional experiments either using Fugene6 (Roche) or Lipofectamine 2000 (Life Technologies) according to the manufacturer's instructions.

EB1/3$^{-/-}$ π-EB1 rescue cells. EB1/EB3$^{-/-}$ cell lines were generated by CRISPR–Cas9-mediated genome editing. Cells were transfected with a mixture of pSpCas9(BB)-2A-GFP (PX458; Addgene 48138)[52] plasmids that encode three different guide RNAs targeting exon 1 of either EB1 or EB3 (guide RNA sequences are included in Supplementary Table 1). GFP-positive cells were single-cell sorted into 96-well plates, and individual clones were analysed by immunofluorescence, immunoblotting and genomic PCR (Supplementary Table 1). EB1/3$^{-/-}$ π-EB1 rescue cells were generated by transfection of π-EB1 constructs followed by selection as described above.

Detailed methods pertaining to the generation of π-EB1 cells are made available on the Protocol Exchange[53].

EB1/3 immunofluorescence. Cells grown on clean no. 1.5 glass coverslips (64–0713, Warner Instruments) were fixed in −20 °C methanol for 10 min, washed with PBS and blocked with blocking buffer (PBS, 2% BSA, 0.05% Tween 20) for 30 min. Mouse anti-EB1 (BD Biosciences clone 5/EB1) and rat anti-EB3 (KT36, Absea) antibodies were diluted in blocking buffer, and 50 μl drops were spotted on a sheet of parafilm in a humidified chamber. Coverslips were placed on top of these droplets (cells facing down), and incubated for 1 h at room temperature, after which the coverslips were washed 3 times in PBS, 0.05% Tween 20. Fluorescent secondary antibodies (Alexa488-conjugated or Alexa568-conjugated goat anti-mouse or goat anti-rat antibodies, Invitrogen) were diluted in blocking solution, and coverslips were incubated and washed as above. Coverslips were dehydrated by brief immersion in 70% ethanol followed by 100% ethanol, air dried and mounted in Mowiol mounting medium (0.1 M Tris-HCl pH 8.5, 25% glycerol, 10% Mowiol 4–88). Detailed information on all antibodies used in this study is included in Supplementary Table 1.

In vitro binding assays and native PAGE. GST-tagged and 6xHis-tagged proteins were produced in *Escherichia coli* BL21 using standard protocols. In brief, bacteria were lysed by three freeze–thaw cycles in dry-ice in lysis buffer (TBS, 0.5% Triton X-100, 1 mM phenylmethylsulfonyl fluoride (PMSF), 0.5 mg ml^{-1} lysozyme) followed by DNAse treatment (1 μg ml^{-1}). Lysates were cleared by centrifugation at 16,000 g for 10 min at 4 °C, and incubated with glutathione sepharose (GE Healthcare), or Talon resin (Clontech). Affinity resins were washed twice with low salt buffer (TBS, 0.1% Triton X-100, 5 mM 2-mercaptoethanol), three times with high salt buffer (TBS, 650 mM NaCl, 0.1% Triton X-100, 5 mM 2-mercaptoethanol). For purification of LOV2-containing constructs, an additional incubation step with low salt buffer containing 5 mg ml^{-1} riboflavin 5′-phosphate (FMN) to ensure stoichiometric loading of the LOV2 domain with the FMN co-factor. Proteins were eluted in low salt buffer containing either 25 mM reduced glutathione (pH 8.5), or 150 mM imidazole, dialysed and concentrated (Amicon Ultra-15 centrifugal filters, 3000MWCO), and aliquots were snap-frozen in liquid nitrogen.

Interaction between LOV2 and Zdk1 was monitored by discontinuous native PAGE. Purified LOV2 and Zdk1 fusion proteins were mixed and incubated for 30 min at 4 °C, and LOV2–Zdk1 complexes were run on 6% native PAGE gels in Tris-glycine buffer pH 8.3 at 75 V for 2 h. A custom-made 470 nm LED array was placed in front of the electrophoresis tank to photoactivate LOV2 as the proteins migrated through the gel.

To test π-EB1 +TIP binding in vitro, H1299 cells were lysed in ice cold 50 mM Tris-HCl, 150 mM NaCl, 0.1% Triton X-100, containing protease inhibitors (cOmplete Protease Inhibitor Cocktail, Sigma) for 30 min. Lysates were cleared by centrifugation at 13,000 rpm in an Eppendorf microcentrifuge and added to glutathione sepharose beads loaded with GST-EB1N-LZ-LOV2 and 6xHis-Zdk1-EB1C, incubated on ice for 30 min and washed extensively. Bound proteins were analysed by SDS–PAGE, wet transfer to nitrocellulose (GVS, 1212590) for 1 h at 60 V (Bio-Rad Mini Trans-Blot) and chemiluminescent detection with horseradish peroxidase-conjugated secondary antibodies using a Fluorchem Q gel documentation system (92-14116-00, Alpha Innotech) using standard protocols. Primary antibodies were mouse anti-p150^{Glued} (BD Transduction Laboratories) and rat anti-CLASP2 (KT68, Absea).

Microscopy, photoactivation and image analysis. Fluorescent protein dynamics were imaged by spinning disk or total internal reflection fluorescence (TIRF) microscopy on a customized microscope setup essentially as described previously[26,45,54], except that the system was upgraded with a next-generation scientific charge-coupled device (CCD) camera (cMyo, Photometrics) with 4.5 μm pixels that allowed optimal spatial sampling using a ×60 NA 1.49 objective (CFI APO TIRF; Nikon). Global π-EB1 photodissociation was achieved by turning on the 488-nm excitation channel. An irradiance of ~250 mW per cm^2 was sufficient to photoactivate the LOV2 domain, although simultaneous imaging of eGFP-tagged proteins required higher light intensity. Irradiance at the specimen plane was measured using a X-Cite XR2100 light power meter (EXFO Photonic Solutions).

To achieve subcellular π-EB1 photodissociation, a digital micromirror device (Polygon 400, Mightex) equipped with a 470 nm LED was mounted on a Nikon TI auxiliary camera port equipped with a beamsplitter, such that 20% of the light path was diverted for photoactivation and 80% was used for spinning disk confocal microscopy. This also allowed for direct imaging of the reflected illumination pattern to accurately focus and align the Polygon 400, as well as simultaneous imaging and π-EB1 photodissociation. To eliminate scattered photoactivation light

in the imaging channel, the Polygon 400 was operated such that short 10–20-ms pulses of blue light were triggered to occur between image acquisitions. For fast time-lapse experiments (at or above 1 frame per second), the Polygon 400 was directly triggered by the camera using a short delay of a few hundred milliseconds after camera exposure. For slower time-lapse experiments, the camera trigger was used to start a pre-programmed pulse sequence between exposures using an ASI MS2000 Sequencer module.

Image analysis was performed in NIS Elements 4.3 or Fiji[55]. Fluorescence intensities were measured in small regions with a diameter of 3–5 pixels on MT ends that were moved in time with MT growth, and nearby cytoplasm as local background. MT end/cytoplasm ratios were calculated as previously described[56]. A ratio of one indicates no measurable difference between the MT end and the local cytoplasm. MT plus-end tracking of mCherry-EB1N was done using u-track version 2.1.3 (refs [57,58]). 'Comet detection' parameters were adapted to decrease the number of false-positive detections as follows: 'High-pass Gaussian standard deviation': 6; Watershed segmentation 'Minimum threshold': between 6 and 8; and other parameters remained at default settings. Similarly, in the 'Tracking' step, the 'Minimum length of track segments' was set to 4. To not bias average MT growth rates toward shorter tracks, frame-to-frame MT growth rates were extracted from the 'tracksFinal' structure using a custom MatLab script, and frame-to-frame displacements of <0.5 pixels were excluded. Tubulin-mCherry-labelled MTs ends were tracked using the Fiji MtrackJ plugin[59].

To analyse the cell migration response to π-EB1 photodissociation, cells were recorded at 1 frame per minute for at least 30 min to select cells that were actively migrating and to determine the pre-exposure direction of migration. Regions of blue light exposure were manually drawn, roughly targeting the front or side of the migrating cell, and blue light patterns were pulsed at a frequency of 1 Hz. The cell outline was determined by fluorescent signal threshold, and the centroid position was calculated in NIS Elements for each time point. To reduce positional noise of the centroid position due to transient changes in cell shape and protrusive activity, the centroid position was smoothened using a nine-frame running average. The angle between 15-min linear segments along this centroid trajectory and centred on the time of π-EB1 photodissociation (that is, 0 min) was then calculated by linear algebra. Turning away from the light-exposed region was defined as a positive angle.

Statistics and reproducibility. Statistical analysis was done with the Analyse-It plugin for Microsoft Excel. Significance of multiple comparisons was calculated using the Tukey–Kramer honest significant difference (HSD) test after confirming normal distribution of the data by Shapiro–Wilk testing. Least square curve fitting was performed using the Solver plugin in Microsoft Excel[60], and 95% confidence intervals of the fit were calculated as described[61]. Figures were assembled in Adobe Illustrator CS5, and videos were made using Apple QuickTime Pro. Box-and-whisker plots show median, first and third quartile, observations within 1.5 times the interquartile range, and all individual data points. All experiments showing representative gel images or immunoblots (Fig. 1a,g and Supplementary Figs. 1a,b,3a,b and 4a), or representative microscopy data (Figs. 2b,e,3d,4c,e,5b,e,g,h and 6d and Supplementary Figs. 1c,2,3c–e and 4b,c,f) were repeated at least three times with similar results.

Life Sciences Reporting Summary. Further information on experimental design is available in the Life Sciences Reporting Summary.

Code availability. The u-track particle tracking package for MATLAB is available from the Danuser Lab at http://www.utsouthwestern.edu/labs/danuser/software/.

Data availability. Statistical source data for Figs. 1d,f,2a–d,3b,c,f,4b,d,5c,f and 6c and Supplementary Fig. 4e are included in Supplementary Table 3. All other data supporting the findings of this study are available from the corresponding author on reasonable request.

References

49. Akhmanova, A. et al. Clasps are CLIP-115 and -170 associating proteins involved in the regional regulation of microtubule dynamics in motile fibroblasts. *Cell* **104**, 923–935 (2001).
50. Wu, Y. I. et al. A genetically encoded photoactivatable Rac controls the motility of living cells. *Nature* **461**, 104–108 (2009).
51. Strickland, D. et al. TULIPs: tunable, light-controlled interacting protein tags for cell biology. *Nat. Methods* **9**, 379–384 (2012).
52. Ran, F. A. et al. Genome engineering using the CRISPR–Cas9 system. *Nat. Protoc.* **8**, 2281–2308 (2013).
53. van Haren, J. & Wittmann, T. Generation of cell lines with light-controlled microtubule dynamics. *Protoc. Exch.*, https://doi.org/10.1038/protex.2017.155 (2018).
54. Stehbens, S., Pemble, H., Murrow, L. & Wittmann, T. Imaging intracellular protein dynamics by spinning disk confocal microscopy. *Methods Enzymol.* **504**, 293–313 (2012).
55. Schindelin, J. et al. Fiji: an open-source platform for biological-image analysis. *Nat. Methods* **9**, 676–682 (2012).
56. Ettinger, A., van Haren, J., Ribeiro, S. A. & Wittmann, T. Doublecortin is excluded from growing microtubule ends and recognizes the GDP-microtubule lattice. *Curr. Biol.* **26**, 1549–1555 (2016).
57. Matov, A. et al. Analysis of microtubule dynamic instability using a plus-end growth marker. *Nat. Methods* **7**, 761–768 (2010).
58. Jaqaman, K. et al. Robust single-particle tracking in live-cell time-lapse sequences. *Nat. Methods* **5**, 695–702 (2008).
59. Meijering, E., Dzyubachyk, O. & Smal, I. Methods for cell and particle tracking. *Methods Enzymol.* **504**, 183–200 (2012).
60. Stehbens, S. J. & Wittmann, T. Analysis of focal adhesion turnover: a quantitative live-cell imaging example. *Methods Cell Biol.* **123**, 335–346 (2014).
61. Brown, A. M. A step-by-step guide to non-linear regression analysis of experimental data using a Microsoft Excel spreadsheet. *Comput. Methods Prog. Biomed.* **65**, 191–200 (2001).

nature research

Corresponding author(s): Torsten Wittmann

☐ Initial submission ☐ Revised version ☒ Final submission

Life Sciences Reporting Summary

Nature Research wishes to improve the reproducibility of the work that we publish. This form is intended for publication with all accepted life science papers and provides structure for consistency and transparency in reporting. Every life science submission will use this form; some list items might not apply to an individual manuscript, but all fields must be completed for clarity.

For further information on the points included in this form, see Reporting Life Sciences Research. For further information on Nature Research policies, including our data availability policy, see Authors & Referees and the Editorial Policy Checklist.

Experimental design

1. Sample size

Describe how sample size was determined.

No statistical method was used to determine sample size. Sample size was chosen based on previous experience and standards in the field.

2. Data exclusions

Describe any data exclusions.

No data were excluded. Cells imaged and analyzed were chosen based on fluorescent protein expression levels.

3. Replication

Describe whether the experimental findings were reliably reproduced.

All experiments were repeated at lease three times with similar outcome.

4. Randomization

Describe how samples/organisms/participants were allocated into experimental groups.

No randomization of experimental groups was performed.

5. Blinding

Describe whether the investigators were blinded to group allocation during data collection and/or analysis.

Investigators were not blinded during data collection and analysis.

Note: all studies involving animals and/or human research participants must disclose whether blinding and randomization were used.

6. Statistical parameters

For all figures and tables that use statistical methods, confirm that the following items are present in relevant figure legends (or in the Methods section if additional space is needed).

n/a	Confirmed
☐	☒ The exact sample size (*n*) for each experimental group/condition, given as a discrete number and unit of measurement (animals, litters, cultures, etc.)
☐	☒ A description of how samples were collected, noting whether measurements were taken from distinct samples or whether the same sample was measured repeatedly
☐	☒ A statement indicating how many times each experiment was replicated
☐	☒ The statistical test(s) used and whether they are one- or two-sided (note: only common tests should be described solely by name; more complex techniques should be described in the Methods section)
☐	☒ A description of any assumptions or corrections, such as an adjustment for multiple comparisons
☐	☒ The test results (e.g. *P* values) given as exact values whenever possible and with confidence intervals noted
☐	☒ A clear description of statistics including central tendency (e.g. median, mean) and variation (e.g. standard deviation, interquartile range)
☐	☒ Clearly defined error bars

See the web collection on statistics for biologists for further resources and guidance.

Software

Policy information about availability of computer code

7. Software

Describe the software used to analyze the data in this study.	NIS Elements 4.3 Image J/FiJi (latest updated version available at the time) Microsoft Excel 2010 with Analyse-It plug-in (Standard Edition 3.90.7) Matlab R2014b u-track 2.1.3 (particle tracking Matlab code from Danuser lab; details in methods)

For manuscripts utilizing custom algorithms or software that are central to the paper but not yet described in the published literature, software must be made available to editors and reviewers upon request. We strongly encourage code deposition in a community repository (e.g. GitHub). *Nature Methods* guidance for providing algorithms and software for publication provides further information on this topic.

Materials and reagents

Policy information about availability of materials

8. Materials availability

Indicate whether there are restrictions on availability of unique materials or if these materials are only available for distribution by a for-profit company.	No unique / restricted materials were used. Relevant plasmid reagents will be made available on Addgene.

9. Antibodies

Describe the antibodies used and how they were validated for use in the system under study (i.e. assay and species).	All antibody information including dilutions used for immunoblotting and immunofluorescence, and how specific antibodies were validated is included in Supplementary Table 1.

10. Eukaryotic cell lines

a. State the source of each eukaryotic cell line used.	NCI-H1299 (ATCC)
b. Describe the method of cell line authentication used.	STR profiling
c. Report whether the cell lines were tested for mycoplasma contamination.	Cells regularly tested negative for mycoplasma.
d. If any of the cell lines used are listed in the database of commonly misidentified cell lines maintained by ICLAC, provide a scientific rationale for their use.	No cell lines used in this study were found in the database of commonly misidentified cell lines that is maintained by ICLAC and NCBI Biosample.

Animals and human research participants

Policy information about studies involving animals; when reporting animal research, follow the ARRIVE guidelines

11. Description of research animals

Provide details on animals and/or animal-derived materials used in the study.	No animals were used in this study.

Policy information about studies involving human research participants

12. Description of human research participants

Describe the covariate-relevant population characteristics of the human research participants.	This study did not involve human research participants.